Numerical method of lines for the relaxational dynamics of nematic liquid crystals

A. K. Bhattacharjee, Gautam I. Menon, and R. Adhikari
The Institute of Mathematical Sciences, C.I.T. Campus, Taramani, Chennai 600013, India
(Received 30 April 2008; published 19 August 2008)

We propose an efficient numerical scheme, based on the method of lines, for solving the Landau–de Gennes equations describing the relaxational dynamics of nematic liquid crystals. Our method is computationally easy to implement, balancing requirements of efficiency and accuracy. We benchmark our method through the study of the following problems: the isotropic-nematic interface, growth of nematic droplets in the isotropic phase, and the kinetics of coarsening following a quench into the nematic phase. Our results, obtained through solutions of the full coarse-grained equations of motion with no approximations, provide a stringent test of the de Gennes ansatz for the isotropic-nematic interface, illustrate the anisotropic character of droplets in the nucleation regime, and validate dynamical scaling in the coarsening regime.

DOI: 10.1103/PhysRevE.78.026707 PACS number(s): 05.10.−a, 64.60.Cn, 61.30.Jf, 05.70.Fh

I. INTRODUCTION

Liquid crystalline phases of matter are rich in examples of subtle order parameters, complex phase behavior, and exotic defect structures [1]. In the nematic phase of liquid crystals, broken rotational symmetry produces elastic and hydrodynamic modes and topological defects of integer and half-integer charge [2]. Understanding the statics and dynamics of nematics is difficult because the order parameter is neither a scalar or a vector, but a more complicated tensorial quantity constrained by symmetry and normalization [1]. For example, the simplest relaxational dynamics which follows from a time-dependent Ginzburg-Landau equation describing a nematic close to thermal equilibrium entails the solution of a set of five coupled nonlinear parabolic partial differential equations for the independent components of the order parameter tensor $\mathbf{Q}$ [3]. For all but the simplest situations, these equations do not have analytical solutions and thus need to be solved numerically. The efficient numerical computation of the solutions of the relaxational dynamics of nematics—nematodynamics—is the problem addressed here.

In this paper, we propose an efficient numerical scheme, based on the method of lines [4,5], for solving the Landau–de Gennes equations for nematodynamics. The method of lines (MOL) is a powerful technique for discretizing initial-value partial differential equations (PDEs). The essence of the MOL is semidiscretization, where a PDE in spatial and temporal variables is discretized in the spatial variable only. This reduces the PDE to a system of ordinary differential equations (ODEs) in the temporal variable. The great advantage of the MOL is that there are powerful numerical methods implemented in general-purpose numerical libraries for the solution of systems of ODEs. The MOL also provides a great degree of freedom in discretizing space, allowing one to chose from finite-difference, finite-volume, finite-element, spectral collocation, or any other suitable spatial discretization. The strategy of semidiscretization, where the spatial discretization and temporal integration are treated as separate steps, allows for considerable flexibility, as both these operations can be optimized according to the demands of the problem to ensure maximum accuracy at minimum computational cost.

Here we combine a finite-difference spatial discretization with a Runge-Kutta temporal integration to solve the relaxational equations of nematodynamics. We benchmark our method through the study of the following three problems: (a) the isotropic-nematic interface and tests of the de Gennes ansatz, (b) the kinetics of the growth of single nematic droplets in the isotropic phase, and (c) coarsening kinetics following a quench from the isotropic into the nematic phase. To enable a comparison with previously published results our numerical results are in two dimensions, although the method and our code are applicable in one, two, and three dimensions.

Our results are summarized as follows. Our numerical scheme permits a stringent test of the de Gennes ansatz for the uniaxial nematic isotropic interface [3]. We show that in the absence of elastic anisotropy, biaxiality is absent in the interfacial region and that the hyperbolic tangent profile proposed by de Gennes provides an accurate fit to the numerical data. We show next that single nematic droplets placed in an isotropic solvent at isotropic-nematic coexistence coarsen anisotropically [6], with initially circular droplets deforming into more ellipsoidal structures as time evolves. In our study of coarsening upon quenches from the isotropic phase, we observe the characteristic annihilation of integer and half integer charge defects (disclinations) as revealed by schlieren plots. For the coarsening problem, we find that order parameter correlation functions at different times can be rescaled to lie on a master curve and that the coarsening exponent associated with the growing length scales is $\frac{1}{2}$. Our numerical results are in excellent agreement with analytical results where available and consistent with numerical results where such results exist.

We extend the previous results for each of the problems we have studied in significant ways: First, in our study of the isotropic-nematic interface, we work with all five components of the order parameter tensor, in contrast to earlier work which used a maximum of three. This enables us to study a variety of more complex situations including curved interfaces and arbitrary anchoring conditions. Second, our study of nematic droplets needs no additional anchoring free energies, such as, for example, the Rapini-Papoular free energy. Interfacial properties like the surface tension thus need

not be assumed, but follow naturally from our calculation. Finally, our study of coarsening employs the full Ginzburg–Landau–de Gennes free energy. In contrast, all previous work has either used a purely director-based description or a symmetry motivated cell-dynamical system, believed to be asymptotically equivalent to the nematic coarsening problem.

In Sec. II, we summarize the order parameter description of nematics in terms of the symmetric, traceless order parameter tensor $Q_{\alpha\beta}$. We discuss the Landau–de Gennes free energy functional describing the free energy associated with order parameter configurations, the phase diagram for the free energy, and the equations of relaxational dynamics. In Sec. III we present the MOL scheme for partial differential equations and show how it may be applied to nematodynamics. In Sec. IV we discuss each of the applications described above in some detail, presenting our numerical results. We conclude by describing extensions of the present method to other problems in the dynamics of nematic liquid crystals and compare our method with other methods available in the literature.

II. RELAXATIONAL DYNAMICS

Orientational order in the nematic phase is quantified through a second-rank, symmetric traceless tensor $Q_{\alpha\beta}$ [1]. The principal axes of this tensor, obtained by diagonalizing $\mathbf{Q}$, specify the direction of ordering. The principal values represent the strength of ordering. Locally, nematic order is defined through $\mathbf{Q}(\mathbf{x},t)=\int du\, f(\mathbf{x},\mathbf{u},t)\overleftrightarrow{\mathbf{uu}}\equiv\langle\overleftrightarrow{\mathbf{uu}}\rangle$ where $f(\mathbf{x},\mathbf{u},t)$ is the molecular orientational distribution function at the position $\mathbf{x}$ at time t, which counts the number of molecules with long axis oriented in the direction $\mathbf{u}$, $\overleftrightarrow{X}$ defines the symmetric traceless part of an arbitrary real second rank tensor $\mathbf{X}$ with

$$\overleftrightarrow{X}=\frac{1}{2}(X+X^T)-\frac{1}{d}\mathrm{Tr}(X), \tag{1}$$

where X^T denotes the transpose of the tensor—i.e., $(X^T)_{\alpha\beta}=X_{\beta\alpha}$—and d denotes the dimension. The average $\langle\cdot\rangle\equiv\int du\, f(\mathbf{x},\mathbf{u},t)(\cdot)$.

The three principal axes specify the director $\mathbf{n}$, the codirector $\mathbf{l}$, and the joint normal to these, $\mathbf{m}$. Given the two principal values S and T, the order parameter can be written as

$$Q_{\alpha\beta}=\frac{3}{2}S\left(n_\alpha n_\beta-\frac{1}{3}\delta_{\alpha\beta}\right)+\frac{1}{2}T(l_\alpha l_\beta-m_\alpha m_\beta), \tag{2}$$

where $\alpha,\beta\equiv x,y,z$ and

$$S=\langle P_2(\cos\theta)\rangle=\left\langle\left(\cos^2\theta-\frac{1}{3}\right)\right\rangle, \tag{3}$$

$$T=\langle\sin^2\theta\cos 2\phi\rangle \tag{4}$$

are measures of alignment with $-\frac{1}{3}\leq S\leq\frac{2}{3}$ and $0\leq T<3S$. $S=\frac{2}{3}$ corresponds to the nematic phase whereas $S=0$ to the isotropic phase. The (polar) angle between $\mathbf{n}$ and $\mathbf{u}$ is θ, while the (azimuthal) angle between $\mathbf{l}$ and $\mathbf{u}$ is ϕ.

In the uniaxial nematic phase, $T=0$ and the tensor (2) takes the form $\mathbf{Q}=(3/2)S\overleftrightarrow{\mathbf{nn}}$. In the biaxial phase, $\mathbf{Q}=(3/2)S\overleftrightarrow{\mathbf{nn}}+(1/2)T(\mathbf{ll}-\mathbf{mm})$. The tensor $\mathbf{Q}$ is diagonal in a coordinate system aligned with the principal axes:

$$\mathbf{Q}=\begin{pmatrix}-(S+T)/2 & 0 & 0\\ 0 & -(S-T)/2 & 0\\ 0 & 0 & S\end{pmatrix}. \tag{5}$$

In a frame of reference which is not aligned with the principal axes, $\mathbf{Q}$ must be expanded in a set of basis tensors $T^i_{\alpha\beta}$ [7], which are symmetric, traceless, and orthonormal:

$$Q_{\alpha\beta}(\mathbf{x},t)=\sum_{i=1}^{5}a_i(\mathbf{x},t)T^i_{\alpha\beta}. \tag{6}$$

Explicitly, these are $\mathbf{T}^1=\sqrt{\frac{3}{2}}\hat{\mathbf{z}}\hat{\mathbf{z}}$, $\mathbf{T}^2=\sqrt{\frac{1}{2}}(\hat{\mathbf{x}}\hat{\mathbf{x}}-\hat{\mathbf{y}}\hat{\mathbf{y}})$, $\mathbf{T}^3=\sqrt{2}\hat{\mathbf{x}}\hat{\mathbf{y}}$, $\mathbf{T}^4=\sqrt{2}\hat{\mathbf{x}}\hat{\mathbf{z}}$, and $\mathbf{T}^5=\sqrt{2}\hat{\mathbf{y}}\hat{\mathbf{z}}$.

The Landau-Ginzburg free energy functional F [3] is obtained from a local expansion in powers of rotationally invariant combinations of the order parameter $\mathbf{Q}(\mathbf{x},t)$:

$$\mathcal{F}_h[\mathbf{Q}]=\frac{1}{2}A\mathrm{Tr}\mathbf{Q}^2+\frac{1}{3}B\mathrm{Tr}\mathbf{Q}^3+\frac{1}{4}C(\mathrm{Tr}\mathbf{Q}^2)^2+E'(\mathrm{Tr}\mathbf{Q}^3)^2. \tag{7}$$

To this, nonlocal terms arising from rotationally invariant combinations of gradients of the order parameter must be added [3]:

$$\mathcal{F}_{el}[\partial Q]=\frac{1}{2}L_1(\partial_\alpha Q_{\beta\gamma})(\partial_\alpha Q_{\beta\gamma})+\frac{1}{2}L_2(\partial_\alpha Q_{\alpha\beta})(\partial_\gamma Q_{\beta\gamma}), \tag{8}$$

where α, β, and γ denote the Cartesian directions in the local frame and L_1 and L_2 are elastic constants. Surface terms of the same order in gradients may also be added, but we omit them in the present work.

In the local free energy density, Eq. (7), $A=A_0(1-T/T^*)$, where T^* denotes the supercooling transition temperature. From the inequality $\frac{1}{6}(\mathrm{Tr}\,\mathbf{Q}^2)^3\geq(\mathrm{Tr}\,\mathbf{Q}^3)^2$, higher powers of $\mathrm{Tr}\,\mathbf{Q}^3$ can be excluded for the description of the uniaxial phase. Thus the uniaxial case is described by $E'=0$, whereas $E'\neq 0$ for the biaxial phase. For nematic rodlike molecules $B<0$ whereas for disklike molecules, $B>0$. The quantities C and E' are always taken to be positive to ensure stability and boundedness of the free energy in both the isotropic and nematic phases. The total free energy including local and gradient terms is

$$F=\int d^3\mathbf{x}\left[\frac{1}{2}A\mathrm{Tr}\mathbf{Q}^2+\frac{1}{3}B\mathrm{Tr}\mathbf{Q}^3+\frac{1}{4}C(\mathrm{Tr}\mathbf{Q}^2)^2+E'(\mathrm{Tr}\mathbf{Q}^3)^2+\frac{1}{2}L_1(\partial_\alpha Q_{\beta\gamma})(\partial_\alpha Q_{\beta\gamma})+\frac{1}{2}L_2(\partial_\alpha Q_{\alpha\beta})(\partial_\gamma Q_{\beta\gamma})\right]. \tag{9}$$

The first-order isotropic to uniaxial nematic transition at the critical value $S=S_c$ is obtained from the equations

$$A = \frac{3}{4}CS_c^2 + \frac{9}{4}E'S_c^4, \tag{10}$$

$$B = -\frac{9}{2}CS_c - 9E'S_c^3. \tag{11}$$

The second-order uniaxial-to-biaxial transition at the critical value $S=S_c'$ is obtained from

$$A = -\frac{9}{2}CS_c'^2, \tag{12}$$

$$B = -\frac{45}{4}E'S_c'^3. \tag{13}$$

In the phase diagram of Fig. 1, there are lines separating the nematic phase with $S>0$ from the discotic phase in addition to the isotropic-to-nematic transition lines. There are also two uniaxial to second-order biaxial nematic lines as well as the two first-order isotropic-uniaxial nematic lines. One of these transition lines marks the transition to the nematic phase with $S>0$ and the other to the discotic phase with $S<0$. The four phases meet at the bicritical Landau point $A=B=0$. At the bicritical point, the isotropic-to-nematic transition is second order rather than first order.

In the absence of thermal fluctuations and hydrodynamic flow, the equation of motion of the order parameter can be taken to be relaxational [3],

$$\partial_t Q_{\alpha\beta}(\mathbf{x},t) = -\Gamma_{\alpha\beta\mu\nu}\frac{\delta F}{\delta Q_{\mu\nu}}, \tag{14}$$

with

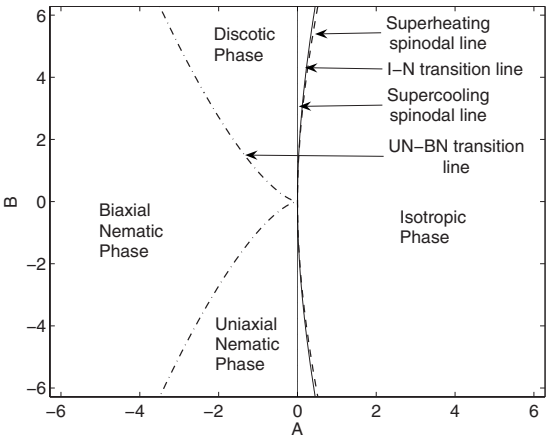

FIG. 1. The mean-field phase diagram obtained from the Landau–de Gennes free energy (7). The phase boundaries are given by solutions of the following algebraic equations: $4B^4E+B^2C(3C^2-144AE')=A(81C^4-864AC^2E'+2304A^2E'^2)$ for the isotropic-to-uniaxial nematic transition, $25A^3E'^2=-18B^2C^3$ for the uniaxial-to-biaxial nematic transition, $A=0$ for the supercooling spinodal, and $9B^4E'+8B^2(C^3-36ACE')=192A(C^2-4AE')^2$ for the superheating spinodal. Here $C=2.67$ and $E'=3.56$.

$$\Gamma_{\alpha\beta\mu\nu} = \Gamma\left(\delta_{\alpha\mu}\delta_{\beta\nu} + \delta_{\alpha\nu}\delta_{\beta\mu} - \frac{2}{3}\delta_{\alpha\beta}\delta_{\mu\nu}\right). \tag{15}$$

The kinetic coefficient $\Gamma_{\alpha\beta\mu\nu}$ ensures that the dynamics preserves the symmetry and tracelessness of the order parameter. In the above, Γ is a constant.

With the choice of the Landau–de Gennes free energy, the equation of motion takes the form

$$\partial_t Q_{\alpha\beta}(\mathbf{x},t) = -\Gamma[(A + C\mathrm{Tr}Q^2)Q_{\alpha\beta}(\mathbf{x},t) + (B + 6E'\mathrm{Tr}Q^3)\overline{Q^2_{\alpha\beta}(\mathbf{x},t)} - L_1\nabla^2 Q_{\alpha\beta}(\mathbf{x},t) - L_2\overline{\nabla_\alpha(\nabla_\gamma Q_{\beta\gamma}(\mathbf{x},t))}]. \tag{16}$$

The equations can be projected onto the tensorial basis $T^i_{\alpha\beta}$ to give a set of equations for the independent components a_i:

$$\partial_t a_i = -\Gamma[(A + C\mathrm{Tr}Q^2)a_i + (B + 6E'\mathrm{Tr}Q^3)T^i_{\alpha\beta}\overline{Q^2_{\alpha\beta}} - L_1\nabla^2 a_i - L_2\overline{T^i_{\alpha\beta}T^j_{\beta\gamma}\partial_\alpha\partial_\gamma a_j}]. \tag{17}$$

Using the orthonormality of the basis tensors $T^i_{\alpha\beta}T^j_{\beta\alpha}=\delta_{ij}$, this can be expanded to the set of five equations:

$$\partial_t a_1 = -\Gamma\left[(A + C\mathrm{Tr}Q^2)a_1 + (B + 6E'\mathrm{Tr}Q^3)\frac{1}{\sqrt{6}}\left(a_1^2 - a_2^2 - a_3^2 + \frac{a_4^2}{2} + \frac{a_5^2}{2}\right) - L_1\nabla^2 a_1 - L_2\left(\frac{1}{6}\nabla^2 a_1 + \frac{1}{2}\partial_z^2 a_1 + \frac{1}{\sqrt{12}}[(\partial_y^2 - \partial_x^2)a_2 + \partial_x\partial_z a_4 + \partial_y\partial_z a_5] - \frac{1}{\sqrt{3}}\partial_x\partial_y a_3\right)\right], \tag{18}$$

$$\partial_t a_2 = -\Gamma\left[(A + C\mathrm{Tr}Q^2)a_2 + (B + 6E'\mathrm{Tr}Q^3)\left(-\sqrt{\frac{2}{3}}a_1 a_2 + \frac{a_4^2}{\sqrt{8}} - \frac{a_5^2}{\sqrt{8}}\right) - L_1\nabla^2 a_2 - L_2\left(\frac{1}{\sqrt{12}}(\partial_y^2 - \partial_x^2)a_1 + \frac{1}{2}[(\partial_x^2 + \partial_y^2)a_2 + \partial_x\partial_z a_4 - \partial_y\partial_z a_5]\right)\right], \tag{19}$$

$$\partial_t a_3 = -\Gamma\left[(A + C\mathrm{Tr}Q^2)a_3 + (B + 6E'\mathrm{Tr}Q^3)\left(-\frac{2a_1a_3}{\sqrt{6}} + \frac{a_4a_5}{\sqrt{2}}\right) - L_1\nabla^2 a_3 - L_2\left(-\frac{1}{\sqrt{3}}\partial_x\partial_y a_1 + \frac{1}{2}[(\partial_x^2 + \partial_y^2)a_3 + \partial_y\partial_z a_4 + \partial_x\partial_z a_5]\right)\right], \tag{20}$$

$$\partial_t a_4 = -\Gamma\left[(A + C\mathrm{Tr}Q^2)a_4 + (B + 6E'\mathrm{Tr}Q^3)\left(\frac{a_1a_4}{\sqrt{6}} + \frac{a_2a_4}{\sqrt{2}} + \frac{a_3a_5}{\sqrt{2}}\right) - L_1\nabla^2 a_4 - L_2\left(\frac{1}{\sqrt{12}}\partial_x\partial_z a_1 + \frac{1}{2}[(\partial_x^2 + \partial_z^2)a_4 + \partial_x\partial_z a_2 + \partial_y\partial_z a_3 + \partial_x\partial_y a_5]\right)\right], \tag{21}$$

$$\partial_t a_5 = -\Gamma\left[(A + C\mathrm{Tr}Q^2)a_5 + (B + 6E'\mathrm{Tr}Q^3)\left(\frac{a_1a_5}{\sqrt{6}} + \frac{a_3a_4}{\sqrt{2}} - \frac{a_2a_5}{\sqrt{2}}\right) - L_1\nabla^2 a_5 - L_2\left(\frac{1}{\sqrt{12}}\partial_y\partial_z a_1 + \frac{1}{2}[(\partial_y^2 + \partial_z^2)a_5 - \partial_y\partial_z a_2 + \partial_x\partial_z a_3 + \partial_x\partial_y a_4]\right)\right]. \tag{22}$$

Note that these equations are parabolic, nonlinear, contain anisotropic gradient terms and are coupled strongly to each other. The efficient computation of the solutions to these equations in a variety of physical situations is described in succeeding sections of this paper.

III. METHOD OF LINES DISCRETIZATION

The equations for the relaxational dynamics of the orientational order parameter presented in the previous section are a set of five coupled nonlinear parabolic differential equations. No analytical solutions are available for these equations in general, and efficient and accurate numerical methods must therefore be sought. Below we present such a method, based on the strategy of semidiscretization, whereby an initial value PDE is discretized only in the spatial variables to yield a set of coupled ODEs. These ODE's can be solved using powerful general purpose solvers.

In the literature, this semidiscretization strategy goes by the name of the "method of lines" [4,5], since the solutions are obtained along fixed lines in the space-time plane. To illustrate this, consider a parabolic initial-value problem in a single spatial variable x, the diffusion equation for a scalar $\psi(x,t)$:

$$\partial_t\psi(x,t) = D\nabla^2\psi(x,t). \tag{23}$$

The MOL discretization proceeds by restricting the field $\psi(x,t)$ to a set of N discrete "collocation" points $x_n = n\Delta x$, $n = 1,2,\ldots,N$, spaced Δx apart, and then uses a discrete approximation for the Laplacian based on these points. The simplest of these approximations is based on local polynomial interpolation resulting in finite-difference schemes [5]. However, the MOL is not restricted to finite differences. When high accuracy is needed, global interpolation based on trigonometric or Chebyshev polynomials can be used to generate spectral approximations of derivatives [8]. When conservation laws need to be respected, finite-volume approximations to the derivatives can be used [9]. In complicated geometries, a finite-element discretization may be the most appropriate. In this example, the simplest approximation is based on nearest-neighbor finite differences, for which

$$(\nabla^2\psi)(x_n) = \frac{1}{(\Delta x)^2}[\psi(x_{n+1}) - 2\psi(x_n) + \psi(x_{n-1})] + O((\Delta x)^2). \tag{24}$$

Inserting this into the diffusion equation, we obtain a set of coupled ordinary differential equations:

$$\partial_t\psi(x_n,t) = \frac{1}{(\Delta x)^2}[\psi(x_{n+1}) - 2\psi(x_n) + \psi(x_{n-1})]. \tag{25}$$

This coupled set of ordinary differential equations, together with initial and boundary conditions, can now be integrated with a suitable numerical integration scheme which ensures accuracy, efficiency, and stability. It is at this stage that the flexibility of the MOL is most apparent, since any number of numerical integration schemes can be implemented without affecting the spatial discretization. Depending on the nature of the system of ODEs, the optimal choice may be either an explicit scheme, an implicit scheme, or one which is designed to handle stiffness. In the above example, for instance, it is well known that an explicit Euler integration scheme leads to an instability unless the time step Δt is constrained by the Courant-Friedrichs-Lewy condition $\Delta t < (\Delta x)^2/2D$ [5]. In contrast, an implicit integration scheme based on the trapezoidal rule gives the stable Crank-Nicolson update [5]. In general, semidiscretization followed by numerical quadrature provides an elegant way of deriving many of the well-known schemes for parabolic PDEs.

The practical implementation of PDE solvers using the MOL discretization is simple since the spatially discretized ODE system can be passed directly to a general purpose ODE solver. The complexity, both algorithmic and computational, in the numerical integration can thereby be transferred directly to the ODE solver library.

We have followed the MOL discretization to construct a solver for PDEs describing the dynamics of the orientational order parameter presented in the previous section. We have used standard nearest-neighbor second-order accurate finite-difference formulas for first and second derivatives in the spatial discretization [10]. More accurate difference approximations to derivatives can be obtained using Fornberg's general formula [11]. For the temporal integration, we have used the ODE solver routines in the GNU Scientific Library. For the problems we study here, we find that an explicit multistage integrator gives a good compromise between accuracy, stability, and computation expense.

Finally, it should be mentioned that the MOL discretization is not restricted to parabolic initial-value problems, but also applies to hyperbolic and mixed parabolic-hyperbolic PDEs [4]. This allows the method described in this paper to be extended to situations where effects of advection from hydrodynamic flow need to be accounted for.

IV. APPLICATIONS

In this section we report benchmarking results using the methodology described in the previous section for the following experimentally relevant situations: the properties of the isotropic-nematic interface at coexistence, the kinetics of droplet evolution between the binodal and spinodal lines, and spinodal decomposition into the nematic phase. In each case, we compare our numerical results with available analytical and numerical results in the literature.

A suitable nondimensionalization of the equations of motion before they are discretized is essential for controlling artifacts and error introduced by the discretization. For our problem, we nondimensionalize the governing equations (16) using the values of dimensionful quantities at coexistence ($T=T_c$). The resulting dimensionless quantities are superscripted with an asterisk, while the dimensionful quantities are subscripted with c. We nondimensionalize the order parameter $Q^*_{\alpha\beta}=Q_{\alpha\beta}/S_c$ by the value of the strength of ordering at coexistence, $S_c=-2B/9C$. The nondimensionalized strength of ordering is then $S^*=S/S_c=3(1+\sqrt{1-24AC/B^2})/4$. The gradient terms in the free energy are nondimensionalized by the length $l_c=\sqrt{54C(L_1+2L_2/3)/B^2}$, which is related to the width of the isotropic-nematic interface at coexistence. The free energy is nondimensionalized as $F^*=F/F_c$, where $F_c=9CS_c^4/16$ is proportional to the free energy barrier between the isotropic and nematic minima at coexistence. Finally, time is nondimensionalized by the characteristic relaxation time $\tau=(\Gamma F_c)^{-1}$.

To solve the equations of motion Eq. (17), we choose the discretization length $\Delta x=\Delta y=1$ and the integration time step $\Delta t=1$. These define simulation units of length and time. To ensure that discretization errors and artifacts are kept to a minimum, the discretization length must be much smaller than the characteristic length $\Delta x=\Delta y \ll l_c$. The integration time step must be much smaller than the characteristic time scale $\Delta t \ll \tau$. The dimensionless discretization scales must then satisfy $\Delta x^*=\Delta x/l_c \ll 1$, $\Delta y^*=\Delta y/l_c \ll 1$, and $\Delta t^*=\Delta t/\tau \ll 1$. Our simulations are performed maintaining the above conditions, on grid sizes ranging from 32×32 to 256×256, with periodic boundary conditions, using the fourth-order Runge-Kutta method as implemented in the GNU Scientific Library for the ODE solver.

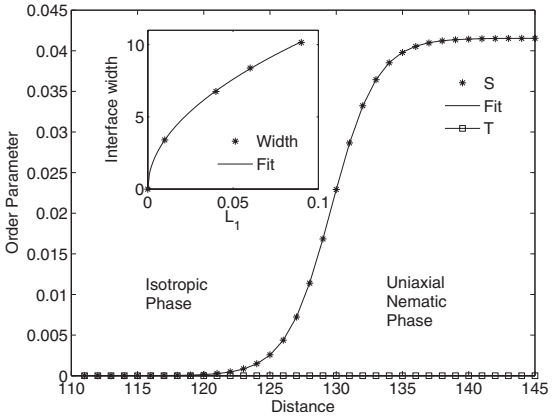

FIG. 2. Variation of the degree of alignment (S) and biaxiality (T) across the nematic-isotropic interface with planar anchoring. Symbols represent numerical data; solid curves are the de Gennes ansatz (26). The numerical parameters are $A=0.0035$, $B=-0.5$, $C=2.67$, $E'=0$, $L_1=0.01$, $L_2=0$, $\Gamma=1/20$, grid size 8×512, and nematic strip width=256. The inset shows the variation of the interfacial width with the elastic constant L_1. The expected quadratic variation is accurately reproduced.

A. Isotropic-nematic interface at coexistence

The isotropic-nematic interface was studied in a seminal paper [3] by de Gennes within the framework of a Landau-Ginzburg description. To render the problem analytically tractable, de Gennes made a specific assumption regarding the variation of the components of the order parameter across the interface. For an infinitely extended interface where, by homogeneity, variations perpendicular to the interface alone are allowed, de Gennes assumed that the only quantity which changed across the interface was the strength of ordering S. In the de Gennes ansatz which assumes the absence of elastic anisotropy, there is no biaxiality and no variation of the director across the interface. This reduces a problem with five degrees of freedom to a more manageable problem involving only a single degree of freedom. The variation of the ordering strength S along the coordinate z normal to the interface located at z_0 can then be obtained analytically as

$$S(z)=\frac{S_c}{2}\left(1-\tanh\frac{z-z_0}{w}\right), \tag{26}$$

where $w=\sqrt{2}/S^*$ is the nondimensional interfacial width.

We have verified this remarkable ansatz with a direct numerical solution. In our numerical calculations, a strip of nematic interface was sandwiched between two isotropic domains with periodic boundary conditions. The system was then allowed to relax to the minimum of the free energy. The parameters were chosen such that the width $w \gg \Delta z=1$, ensuring that discretization errors were kept to a minimum.

The resulting profiles for the variation of S and T are shown in Fig. 2. The values obtained for T are consistent

with de Gennes' assumption of vanishing biaxiality. The variation of S at each of the two isotropic-nematic interfaces was fitted, using the least-squares method, to the analytical profile, with saturation value of the order S_c, the location of the interface z_0 and the interface width w as fitting parameters. As shown in the inset to Fig. 2, fitted values of w agree remarkably well with the analytic result for a range of parameter values. The agreement is accurate to within a fraction of a percent. Similar results were obtained for the saturation value of the order parameter. This benchmark clearly demonstrates the accuracy of the MOL scheme in reproducing the equilibrium limit of Eq. (14).

The de Gennes ansatz also predicts that the energies of planar and homeotropic anchoring are identical when elasticity is isotropic ($L_2=0$). We compared the value of the free energies of the interface for both planar and homeotropic anchoring of the director. To machine precision, these answers are identical. Our results for this problem represent a direct verification of the de Gennes ansatz, retaining all degrees of freedom of the orientational tensor.

B. Nematic droplet in an isotropic background

Since the isotropic-nematic transition is first order, there exists a regime of parameters where the kinetics proceeds by nucleation. In the phase diagram of Fig. 1 this regime is bounded by the binodal and spinodal lines. A droplet of nematic phase in an isotropic background shrinks if it is smaller than a critical size R_c. Droplets which are larger than R_c grow in size until they expand to the size of the system. A droplet of size R_c is thus metastable.

The development in time of a fluctuation-induced droplet is a key factor in determining the nucleation rate [6]. Unlike conventional isotropic fluids, the nucleus in a nematic is not expected to be spherical [12]. Allowing the shape to deviate from perfect sphericity reduces the total energy, which is a sum of the elastic energy associated with the director deformation in the bulk and a surface energy associated with the anchoring condition at the interface of the droplet. Thus, determining the droplet shape of least energy involves a minimization over the strength of ordering as well as the director degrees of freedom [13–15].

In our simulations we have studied the time evolution of droplet shapes. For studying conformational changes, our initial condition was chosen to be $S=S_c$, with the director anchored at an angle of $\pi/4$ with the nematic-isotropic interface inside the droplet. We took $S=0$ in the isotropic region. We relaxed the system at a temperature intermediate between the binodal and spinodal temperatures.

For droplets larger than the critical radius, the nematic region was observed to grow in size, finally evolving into the full nematic state. For the parameters used, the alignment of the director did not change significantly during the evolution of the droplet. Figure 3 shows three stages in the evolution of a single, initially circular droplet, illustrating how the droplet shape evolves into an elongated ellipsoidal form. In the absence of elastic anisotropy, $L_2=0$, the droplet remains circular. In the presence of elastic anisotropy, the droplet orients along the direction of nematic order for planar anchoring ($L_2>0$) and perpendicular to it for homeotropic anchoring ($L_2<0$).

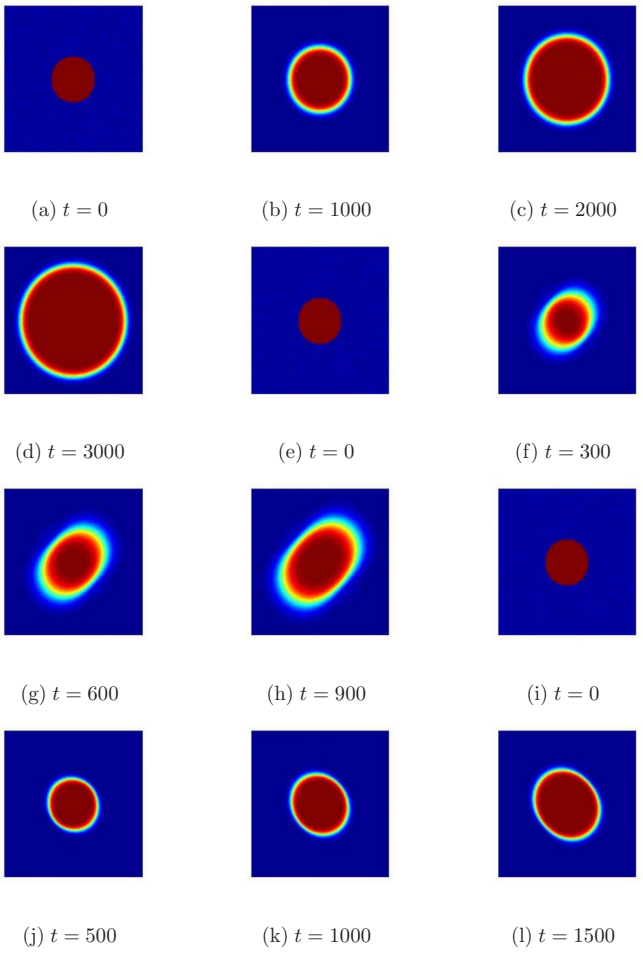

FIG. 3. (Color online) Time evolution of the degree of alignment in the relaxation of a nematic droplet. The initially circular droplet develops an anisotropy and becomes elliptical, the two-dimensional analog of the ellipsoidal droplets (tactoids) seen in three dimensions. (a), (e), and (i) show the circular droplet at time $t=0$. The time evolution with $L_2=0$ of the circular droplet are shown in (b), (c), and (d). The elliptical conformations with $L_2>0$ are shown in (f), (g), and (h). These have aspect ratio 1.1191, 1.3046, and 1.5037, respectively. With $L_2<0$ conformations are shown in (j), (k), and (l). These have aspect ratio 1.0122, 1.0718, and 1.1316, respectively. The numerical parameters are $A=0.001$, $B=-0.5$, $C=2.67$, $E'=0$, $L_1=0.0236$, $\Gamma=1.0$, grid size 128×128, and the droplet radius=20. The elastic constant $L_2=10L_1$ for the $L_2>0$ and $L_2=-L_1$ for $L_2<0$.

In our numerics, we quantify this geometrical change through measurements of the change in the aspect ratio. The aspect ratio, defined as the ratio of the major to minor axis of the ellipse, is indicated in the caption to Fig. 3. This is calculated by extracting a contour at a fixed value of S (say, $S_c/2$) and fitting it with an ellipse.

To the best of our knowledge, there are no analytical expressions for order parameter variations for nematic droplets. Thus, our results cannot be compared directly against analytical theory. However, the results obtained are in

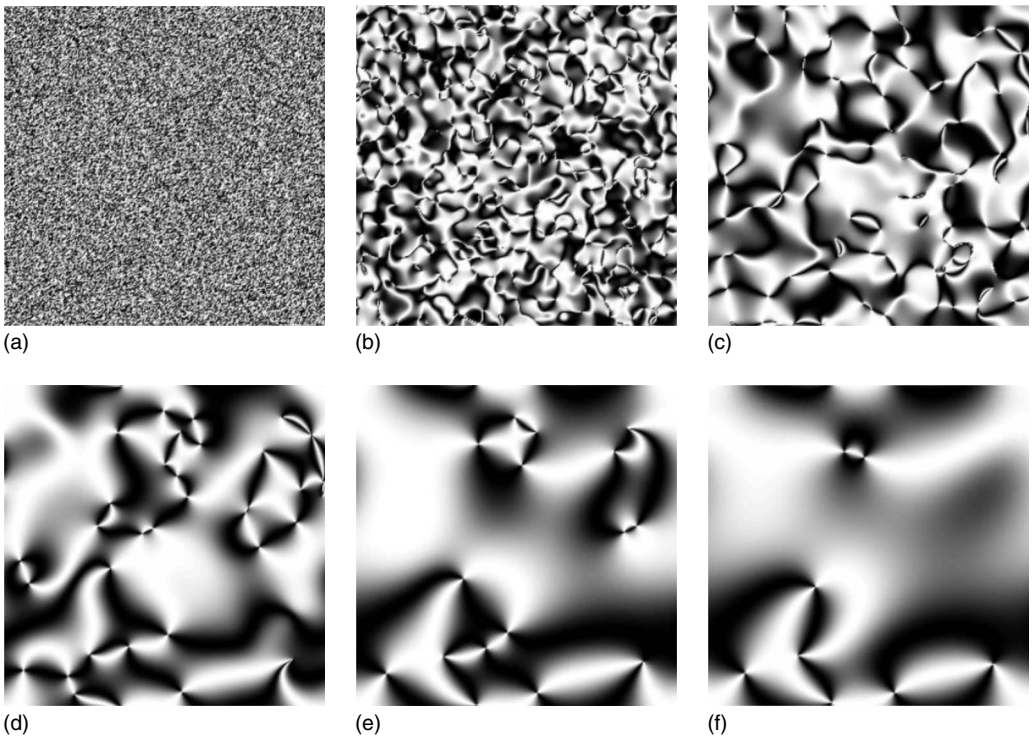

FIG. 4. Schlieren textures in a coarsening nematic. Topological defects of both integer charge [top right in (c) and (d)] and half-integer charge (throughout) are observed in the simulations. (a) shows the random configuration at time $t=0$. (b), (c), (d), (e), and (f) show the dynamics at different times $t=10^3$, 5×10^3, 2×10^4, 6×10^4, and 10^5, respectively. The parameters chosen are $A=-0.1$, $B=-0.5$, $C=2.67$, $E'=0.0$, $L_1=1.0$, $L_2=0$, $\Gamma=1.0$, and grid size 256×256 for 10^5 time steps.

qualitative agreement with previous work on the shape of nematic droplets as a function of anchoring strength [13–16].

C. Spinodal coarsening

In the previous section, we studied the dynamics of droplets when the quench was to a temperature between the binodal and the spinodal. For a quench below the spinodal temperature, the isotropic phase becomes locally unstable to a nematic perturbation and the system proceeds to the nematic phase by spinodal decomposition. Coherent regions of local nematic order develop in time, with a distinct axis of order in each of these domains. Topological defects form at the intersections of these differently ordered domains. Coarsening proceeds through the annihilation of topological defects, increasing the correlation length of local orientational order.

To study the coarsening kinetics, we start from a random initial configuration where we draw the order parameters S and T randomly from a Gaussian random variable with variance proportional to F_c, ensuring that $0<T<S$. We obtain $\cos\theta$ from an uniform distribution between -1 and 1, and choose ϕ similarly between 0 and 2π to generate the director, codirector, and the joint normal. We then relax the system from this initial condition at a temperature below the supercooling spinodal temperature. The data presented below are averaged over 100 different initial conditions for a 256×256 system with periodic boundary conditions.

From the coarsening simulations we obtain the strength of ordering, the biaxiality, and the director. The director is used to construct the schlieren plots shown in Fig. 4. These plots are constructed by first projecting the director onto the x-y plane, finding the angle χ made by this projection with an arbitrary axis (say, the x axis), and then computing $\sin^2(2\chi)$. The presence of both integer and half-integer defects is clearly visible in these plots as the meeting points of four and two dark brushes, respectively. In the corresponding plots for the strength of ordering, the defects are clearly visible as localized regions where S rapidly decreases. This is the core region of the topological defect, shown in Fig. 5. We confirm the surprising finding that there is strong biaxial ordering inside the defect core [17]. These results are in perfect qualitative agreement with both theoretical predictions and previous numerical results [17].

To make a quantitative comparison with previous work, we compare results for the time development of correlation functions during coarsening. We calculate the real-space correlation function

$$C(\mathbf{r},t)=\frac{\int d^3\mathbf{x}Q_{\alpha\beta}(\mathbf{x},t)Q_{\beta\alpha}(\mathbf{x}+\mathbf{r},t)}{\int d^3\mathbf{x}Q_{\alpha\beta}(\mathbf{x},t)Q_{\beta\alpha}(\mathbf{x},t)} \tag{27}$$

and its Fourier transform

$$S(\mathbf{k},t)=\frac{Q_{\alpha\beta}(\mathbf{k},t)Q_{\beta\alpha}(-\mathbf{k},t)}{\int d^3\mathbf{k}Q_{\alpha\beta}(\mathbf{k},t)Q_{\beta\alpha}(-\mathbf{k},t)}. \tag{28}$$

Theoretical predictions and analytical work have verified that these correlation functions have a scaling form $C(r,t)=\mathcal{F}[r/L(t)]$ and $S(k,t)=L^d(t)\mathcal{G}[kL(t)]$ [18]. Here,

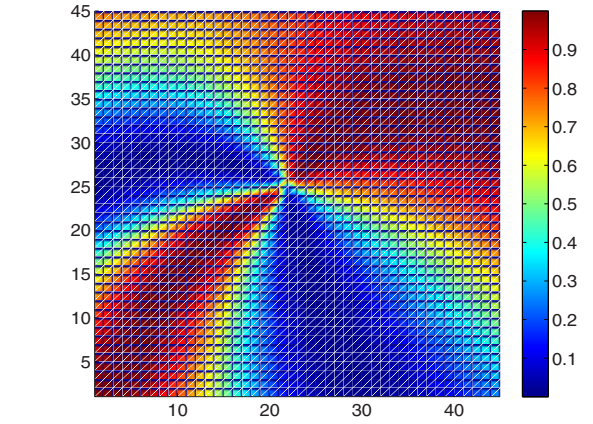

(a)

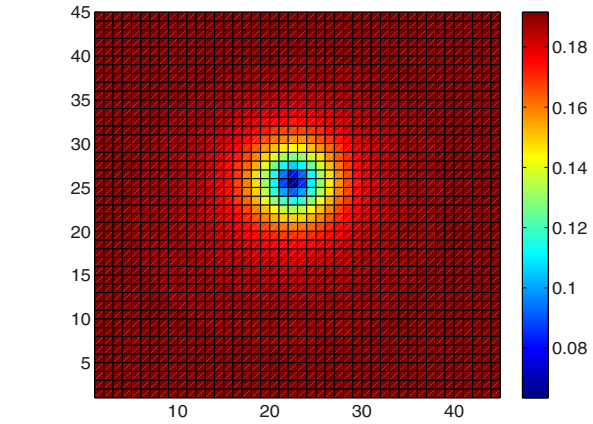

(b)

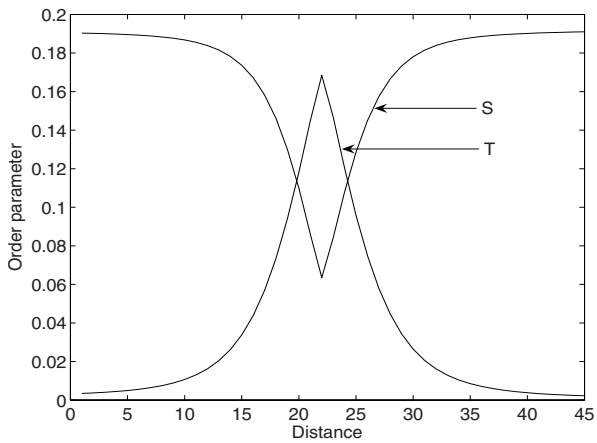

(c)

FIG. 5. (Color online) The schlieren texture around a half-integer charge defect is shown in (a), (b) shows the density plot of the uniaxial order parameter, while (c) exhibits the variation of the uniaxial and biaxial order parameter along a line passing through the defect core. Note the presence of strong biaxiality within the defect core as seen previously [17]. The sharpness of the variation at the core reflects the coarseness of our discretization and would be smoothed out by a finer discretization.

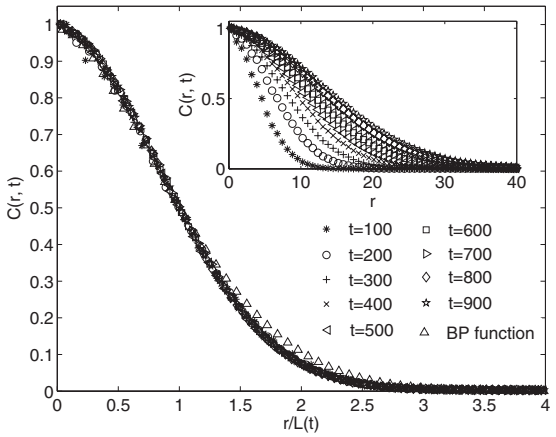

FIG. 6. Data collapse of the direct correlation function $C(r)$ with scaled distance $r/L(t)$ for different times. The symbol Δ depicts the Bray-Puri function [34] for the O(2) vector model: $f_{BP}(x) = B^2(0.5,1.5)F[0.5,0.5,2;\exp(-x^2)]\exp(-x^2/2)/\pi$. The inset shows the unscaled correlation function at different times. Numerical parameters chosen were $A=-0.1$, $B=-0.5$, $C=2.67$, $E'=0$, $L_1=1.0$, $L_2=0$, and $\Gamma=1/20$ on a 256×256 grid.

$C(r,t)=\Sigma_{|\mathbf{r}|=r}C(\mathbf{r},t)$ and $S(k,t)=\Sigma_{|\mathbf{k}|=k}S(\mathbf{k},t)$ are angular averages of the correlation functions in real and Fourier space, respectively. The length $L(t)$ is extracted from the real-space correlation function using the implicit condition $C(r=L(t),t)=1/2$. In Fig. 6 we confirm that the real-space correlation function does indeed scale as expected. Our numerical data for the scaling function are in close agreement with an analytical calculation for the two-component *vector* model due to Bray and Puri [19], although the symmetry of this model is not the same as the tensorial symmetry of the nematic problem. A similar comparison has been made in [20]. In Fig. 7 we show the corresponding scaling of the Fourier-space correlation function. The wave number $\langle k\rangle$ is the root of the second moment of the $S(\mathbf{k},t)$ defined by

$$\langle k\rangle^2 = \frac{1}{L(t)^2} = \sum_{\mathbf{k}} k^2 S(\mathbf{k},t) \Big/ \sum_{\mathbf{k}} S(\mathbf{k},t). \tag{29}$$

The inset shows the growth of the length scale as a function of time. Theoretically, this is expected to grow as a power $L(t)\sim t^{\alpha}$. Our estimate for this exponent is $\alpha=0.5\pm0.005$.

Our results are consistent with both analytical predictions and an earlier numerical simulation. The Fourier-space correlation function is expected to exhibit a short-wavelength scaling $S(k,t)\sim k^{-4}$ known as a generalized Porod's law [18]. We see a clear range of wave numbers where the Porod scaling is obtained. At very short wavelengths, corresponding to the size of the defect core, the Porod scaling breaks down. We see evidence for this as well, where the very highest wave numbers in Fig. 7 show deviations from the Porod scaling. Our numerical results for spinodal decomposition, then, agree both qualitatively and quantitatively with theoretical results and previous numerical work [21]. There are numerical results reported in the literature that are conflicting [22,20]. We indicate possible reasons for this discrepancy in the following section.

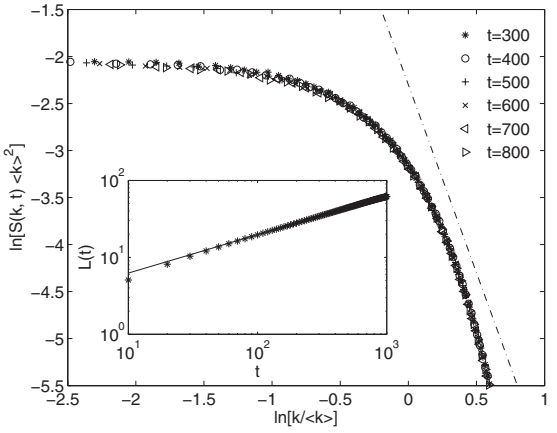

FIG. 7. Data collapse of the structure function $S(k,t)$ at different times. The dash-dotted line has a slope of −4, indicating the validity of the generalized Porod's law for $O(n)$ vector systems. The departure from Porod's law at high k is due to the finite core size of the defects as discussed in the text. The inset shows the time dependence of the correlation length, $L(t)$. The length grows as a power law with an exponent of 0.5. The maximum value of the correlation length is approximately one-fourth the system size, ensuring the absence of finite-size artifacts. Numerical parameters chosen are $A=-0.025$, $B=-0.5$, $C=2.67$, $E'=0$, $L_1=0.1$, $L_2=0$, and $\Gamma=1/20$ on a 256×256 grid.

D. Discussion

For the nematic-isotropic interface, elastic anisotropy ($L_2\neq0$) induces biaxiality near the interface. This problem has been studied using various approximations by several authors. Sen and Sullivan [23] introduced a symmetry-adapted parametrization of the order parameter which reduces the independent degrees of freedom to three. Using this parametrization Popa-Nita and Sluckin [24,25] obtained numerical solutions for the variation of S and T across the interface. The parametrization used in these calculations is only applicable to the cases of planar or homeotropic anchoring at the interface. For a general anchoring condition this parametrization breaks down, as is obvious from the fact that the order parameter has, in general, five independent components.

With the present method, the same problem can be studied without any approximation, retaining all degrees of freedom of the orientation tensor. This allows us to obtain the variation of the order parameter in situations where the symmetry conditions of Sen and Sullivan do not apply. These include curved interfaces and the effect of higher order elasticity.

With regard to the problem of nematic droplets a detailed study becomes possible, especially in three dimensions. Indeed the only numerical work we know of is the Monte Carlo simulation of Cuetos and Dijkstra [6]. The advantage of the Landau–de Gennes approach for this problem is that the free energy of anchoring need not be postulated (as is done when only the director degrees of freedom are retained and a Rapini-Papoular [26] free energy used), but is effectively present in the Landau–de Gennes free energy itself. This is the calculational strategy used by Prinsen and van der Schoot [16]. Nontrivial director configurations have been proposed for different strengths of bulk-to-surface coupling. Such predictions can be verified cleanly with the present method.

For nematic coarsening in three dimensions, simulations within the Landau–de Gennes framework have not been performed so far. The extended nature of topological defects, which are lines rather than points in three-dimensional nematics, makes the dynamics of the coarsening problem quite different from two dimensions. The strength of the Landau–de Gennes approach is particularly clear here. Having access to the strength of ordering makes it easy to locate the defect lines as tubes of minima of the ordering strength. This is considerably easier than using a Burgers-like circuit integral of the director field to locate defects as is done in the work of Zapotocky *et al.* [22].

The dynamics of defect lines has implications in cosmology, where the Kibble mechanism [27] predicts a scaling relation for the number density of defects. Experiments studying the Kibble mechanism in liquid crystals have been performed [28]. However, we know of no numerical study of the Kibble mechanism along the lines proposed here for nematic liquid crystals. This provides further impetus for three-dimensional simulations.

There are two alternatives to the MOL discretization for tensor order parameter descriptions of the nematic phase. These are the cell dynamical scheme of Oono and Puri [29] as implemented by Zapotocky *et al.* [22] and Dutta and Roy [20], and the lattice Boltzmann method of Denniston *et al.* [30]. Our method differs in an important way from both these approaches, in that it provides a direct discretization of the governing equations of motions. In cell-dynamical simulations, a local map is constructed whose fixed points coincide with the extrema of the local part of the free energy. This local map is phenomenological and does not follow from a Landau expansion. The advantage of this method is that it produces sharp interfaces, ensuring a rapid scale separation between the microscopic interfacial length and the macroscopic domain size. In coarsening simulations, this reduces the nonuniversal offset time at which the system enters the scaling regime.

In comparison, the Landau–de Gennes free energy leads to a less sharp interface. Consequently, the structure of the core region of topological defects is different in the two methods, being smaller in cell dynamics and larger in the present method. We see evidence of this in the dynamic structure factor, Fig. 7, where there is a violation of Porod scaling at the highest wave numbers. As shown in Fig. 5 the core region of our defect spans several lattice spacings in each direction. Thus, as regards scale separation between what are microscopic and macroscopic lengths, the cell dynamical scheme fares better.

On the other hand, when physics at the scale of the interface is important, as in the problem of the planar interface and nematic droplets, the MOL discretization offers a clear advantage. Due to the special nature of the cell dynamical Laplacian, it is not clear how to generalize the cell dynamical method to include elastic anisotropy (corresponding to the gradient term with coefficient L_2) or higher-order terms involving antisymmetric contractions. Due to the phenomenological nature of the cell dynamical map, it is difficult to

make direct contact with experiment, a procedure which is straightforward in the MOL when the nondimensionalization we outlined above is applied.

In the lattice Boltzmann method, the governing parabolic equations are replaced by a hyperbolic superset [31] through the introduction of a distribution function for the tensor order parameter. As with cell dynamics, the Landau–de Gennes equations are not solved directly. Rather, lattice Boltzmann relies on a temporal scale separation which allows the hyperbolic equations to mimic parabolic behavior. The lattice Boltzmann method needs to be carefully formulated [32] to avoid the presence of microcurrents, and this procedure appears to be nonuniversal [33]. We find no evidence of spurious microcurrents in the MOL discretization presented here. The lattice Boltzmann method includes the coupling of order parameter and flow. It is entirely straightforward to extend the MOL discretization to include order parameter advection. To include coupling to the fluid momentum, we advocate a hybrid strategy, where the order parameter dynamics including advection is solved by a MOL discretization, but the dynamics of the fluid momentum including order parameter stresses is solved by the lattice Boltzmann method.

In terms of algorithmic complexity, cell dynamics, the lattice Boltzmann method, and the MOL with finite differences appear to be matched, since both use fairly local information to calculate derivatives and involve explicit temporal updates. For N degrees of freedom the algorithmic complexity of all three algorithms is $O(N)$. On the other hand, the storage requirements of the lattice Boltzmann formulation are larger by a factor of 6–9 in two dimensions and about 15–19 in three dimensions. On an Intel(R) Core(TM)2 Duo CPU with speed 2.66 GHz, our code takes 0.33 s for one time step once a lattice size of 256×256.

V. CONCLUSION

This paper has proposed an efficient numerical scheme based on the method of lines for the solving the Landau–de Gennes equations of nematodynamics. The numerical results obtained in previous sections are in excellent agreement with analytical results where available and consistent with previous numerical data. We expect that the method presented here will find broad application in exploring the rich physics of the nematic phase of liquid crystals.

ACKNOWLEDGMENTS

We thank the Indo-French Centre for the Promotion of Advanced Research and the DST, India for support.

[1] P. G. de Gennes and J. Prost, *The Physics of Liquid Crystals*, 2nd ed. (Clarendon Press, Oxford, 1993).
[2] P. Chaikin and T. Lubensky, *Principles of Condensed Matter Physics*, 1st ed. (Cambridge University Press, Cambridge, England, 1995).
[3] P. G. de Gennes, Mol. Cryst. Liq. Cryst. **12**, 193 (1971).
[4] O. A. Liskovets, J. Differ. Equations **1**, 1308 (1965).
[5] R. J. LeVeque, *Finite Difference Methods for Ordinary and Partial Differential Equations, Steady State and Time Dependent Problems* (SIAM, Philadelphia, 2007).
[6] A. Cuetos and M. Dijkstra, Phys. Rev. Lett. **98**, 095701 (2007).
[7] G. Rienäcker, M. Kröger, and S. Hess, Physica A **315**, 537 (2002).
[8] L. N. Trefethen, *Spectral Methods in Matlab* (SIAM, Philadelphia, 2000).
[9] R. J. LeVeque, *Finite Volume Methods for Hyperbolic Problems* (Cambridge University Press, Cambridge, England, 2002).
[10] *Handbook of Mathematical Functions: With Formulas, Graphs, and Mathematical Tables*, edited by M. Abramowitz and I. A. Stegun (Dover, New York, 1964).
[11] B. Fornberg, SIAM Rev. **40**, 685 (1998).
[12] J. D. Bernal and I. Fankuchen, J. Gen. Physiol. **25**, 111 (1941).
[13] C. Herring, Phys. Rev. **82**, 87 (1951).
[14] S. Chandrasekhar, Mol. Cryst. **2**, 71 (1966).
[15] E. G. Virga, *Variational Theories for Liquid Crystals* (Chapman and Hall, London, 1994).
[16] P. Prinsen and P. van der Schoot, Phys. Rev. E **68**, 021701 (2003).
[17] N. Schopohl and T. J. Sluckin, Phys. Rev. Lett. **59**, 2582 (1987).
[18] A. J. Bray, Adv. Phys. **43**, 357 (1994).
[19] A. J. Bray and S. Puri, Phys. Rev. Lett. **67**, 2670 (1991).
[20] S. Dutta and S. K. Roy, Phys. Rev. E **71**, 026119 (2005).
[21] C. Denniston, E. Orlandini, and J. M. Yeomans, Phys. Rev. E **64**, 021701 (2001).
[22] M. Zapotocky, P. M. Goldbart, and N. Goldenfeld, Phys. Rev. E **51**, 1216 (1995).
[23] A. K. Sen and D. E. Sullivan, Phys. Rev. A **35**, 1391 (1987).
[24] V. Popa-Nita and T. J. Sluckin, J. Phys. II **6**, 873 (1996).
[25] V. Popa-Nita, T. J. Sluckin, and A. A. Wheeler, J. Phys. II **7**, 1225 (1997).
[26] A. Rapini and M. J. Papoular, J. Phys. (Paris), Colloq. **30**, C4-54 (1969).
[27] T. W. B. Kibble, J. Phys. A **9**, 1387 (1976).
[28] I. Chuang, R. Durrer, N. Turok, and B. Yurke, Science **251**, 1336 (1991).
[29] Y. Oono and S. Puri, Phys. Rev. Lett. **58**, 836 (1987).
[30] C. Denniston, E. Orlandini, and J. M. Yeomans, Phys. Rev. E **63**, 056702 (2001).
[31] S. Succi, *Lattice Boltzmann Equation for Fluid Dynamics and Beyond* (Oxford University Press, Oxford, 2001).
[32] S. V. Lishchuk, C. M. Care, and I. Halliday, Phys. Rev. E **67**, 036701 (2003).
[33] S. V. Lishchuk, C. M. Care, and I. Halliday, J. Phys.: Condens. Matter **16**, S1931 (2004).
[34] A. J. Bray and S. Puri, Phys. Rev. Lett. **67**, 2670 (1991).